A very deep *Chandra* observation of the giant HII region N11
I. Catalog of sources and X-ray emission from massive stars

Yaël Nazé[1]

GAPHE, Department AGO, Université de Liège, Allée du 6 Août 17 Bat. B5C, B4000-Liège, Belgium

naze@astro.ulg.ac.be

Lida Oskinova

Lehrstuhl Astrophysik der Universität Potsdam, Am Neuen Palais 10, 14469 Potsdam, Germany

You-Hua Chu

Department of Astronomy, University of Illinois, 1002 West Green Street, Urbana, IL 61801, USA

and

Q. Daniel Wang

Department of Astronomy, B619E-LGRT, University of Massachusetts, Amherst, MA 01003, USA

ABSTRACT

A very sensitive X-ray investigation of the giant HII region N11 in the LMC was performed using the *Chandra* observatory. The 300 ks observation, split into 6 equal exposures, reveals X-ray sources with luminosities down to 10^{32} erg s^{-1}. This unique dataset multiplies by more than 5 the number of known point sources in the field. It also uncovers the true extent and detailed spatial properties of the soft, diffuse emissions. The analysis of this deep observation will be reported in a series of papers. This first instalment deals with the data reduction and the establishment of a source catalog. It also details the analysis of the point sources associated with massive stars.

Subject headings: ISM: individual objects: LMC N11 – Magellanic Clouds – galaxies: star clusters – X-rays: stars

---

[1]Postdoctoral Researcher FRS-FNRS

1. Introduction

In the Large Magellanic Cloud (LMC), N11 is the second largest HII region, just after the well-known behemoth 30 Doradus. Star formation has been very active in N11, with no less than four recognized OB associations: LH9, LH10, LH13, and LH14 (Lucke & Hodge 1970). Stars in these clusters have interacted with the surrounding interstellar material. Notably, the winds and supernovae explosions of the massive stars in LH9 have gradually carved a cavity, giving rise to an expanding superbubble some 120pc in size (Rosado et al. 1996). This expansion has probably triggered the formation of LH10 at the periphery of the superbubble (Walborn & Parker 1992). In turn, the massive stars of LH10 are now beginning to blow bubbles (Nazé et al. 2001), further triggering new star formation in their surroundings (Barbá et al. 2003).

N11 thus clearly represents one of the best places to study the interplay between stars and the interstellar medium. This interaction, often violent, is best studied in X-rays. However, sensitive X-ray observations of the LMC are difficult to obtain. Using ROSAT-PSPC, Mac Low et al. (1998) was the first to report the detection of X-rays in the direction of N11. Their 30 ks ROSAT exposure revealed the presence of extended areas of diffuse emission, with the brightest sources associated with the supernova remnant N11L and with the LH9 cavity. Further investigation was performed with *XMM-Newton*, which provided the first detection of point sources in the field (Nazé et al. 2004). While stars in LH9 remained unresolved, the 30 ks *XMM* exposure unveiled in LH10 a mix of diffuse emission and point sources associated with some of the most massive stars of the cluster.

However, a detailed X-ray analysis of N11 requires a combination of both sensitivity and high spatial resolution, which had not been obtained up to now. This is why we have performed a new, deep X-ray investigation of N11, using the *Chandra* observatory. This unique dataset will be the subject of a series of papers. In addition to this one, two additional papers will report on the X-ray emission of the supernova remnant N11L and the detailed analysis of the diffuse emissions, respectively. This first paper is organized as follows: Section 2 presents the data and their reduction, Section 3 further introduces the catalog of X-ray sources and their global properties, Sections 4 and 6 deals with X-ray binaries and 'normal' massive stars, respectively, Section 7 reports on the preliminary analysis of the diffuse emissions, and Section 8 finally summarizes our results.

2. Observations and Data Reduction

The data on N11 were taken in six separate observations of duration 40–50 ks, as summarized in Table 1. Our data reduction and analysis are based on the pipeline products of the observations and on our own IDL-based analysis tools (e.g., Wang 2004) as well as the latest version of the official software for the *Chandra* Interactive Analysis of Observations (CIAO; version beta1-4.0) together with the calibration database (caldb 3.4.0) and other publicly available routines (e.g., XSPEC). We remove time intervals of significant background flares with count rates deviating more than 3σ or a factor of $\gtrsim 1.2$ from the mean rate of individual observations, using Maxim Markevitch's light-curve cleaning routine "lc_clean". This cleaning, together with a correction for the dead time of the six observations, resulted in a total 283 ks exposure for subsequent analysis.

We estimate the non-X-ray background contribution, using the ACIS stowed background database, which has been processed with CTI and gain corrections[1]. The background level in each chip of individual observations is further normalized according to the ratio of its count rate to that of the stowed data in the 10–12 keV band, where events are almost completely due to the non-X-ray background. Compared to the stowed data, the background in our observations is a factor of 1.32 higher with rms equal to 0.04. This factor is also used for the normalization of the background contributions in diffuse X-ray spectral analysis.

We construct effective exposure maps in the four bands: 0.5–1, 1–2, 2–4, and 4–8 keV. The construction of these broad band exposure maps assumes a power law spectrum of photon index 1.7 and accounts for the telescope vignetting and bad pixels as well as the quantum efficiency variation of the instrument, including the time-dependent sensitivity degradation, which is particularly important at low energies ($\lesssim 1.5$ keV). Fig. 1 shows such a merged effective exposure map, illustrating the features of the bad pixel removal, CCD gaps, observation dithering, etc. as well as the overall field coverage. In each band, we construct an X-ray intensity map by first subtracting the non-X-ray background from the detected events and then dividing the net counts by the effective exposure.

We search for X-ray sources in the three broad bands: (S) 0.5–2, (H) 2–8, and (B) 0.5–8 keV. A combination of source detection algorithms are applied: wavelet, sliding-box, and maximum likelihood centroid fitting (Wang 2004). Our final source list contains sources with local false detection probability less than 10^{-6} (due to the Poisson fluctuation above the local sky background). The sensitivity of the source detection depends on the size of the point spread function as well as the local background level and effective exposure, which

[1]following the procedure described on http://cxc.harvard.edu/contrib/maxim/acisbg/

all vary with position, especially with the off-axis angle of the observation. The source detection, though optimized for point-like sources, includes a few strong peaks of the diffuse X-ray emission, chiefly associated with the SNR N11L, about $\sim 7'$ west of the field center (for more on this source, see Williams et al., or paper II, in prep).

Source count rates are estimated within the 70% energy-encircled radius (EER) of the point spread function, depending on the off-axis angle. To study diffuse X-ray emission, we remove a region of twice the 70% EER around each source with a count rate (CR) $\lesssim 0.01$ cts s^{-1}. For brighter sources, a factor of $1 + \log(CR/0.01)$ is further multiplied to the source-subtraction radius. For visual presentation of smoothed diffuse X-ray intensity maps, we replace the source-removed region with values estimated from data in surrounding bins.

We extract an ACIS spectrum for each source detected with $S/N > 10$. The on-source spectral extraction circle has the same radius as used for the source removal, while the local background spectrum is estimated from a concentric annulus with the inner radius equal to $2\times$ the circle radius and the outer radius twice larger, but with a minimum value of $50''$. Detected sources are removed from the background region. After a normalization that accounts for bad pixels and boundaries of the CCDs as well as the source removal, the background spectrum is subtracted from the on-source spectrum in XSPEC. We obtain the averaged response matrices of each source spectrum, using the weights derived from on-source 0.5–2 keV band counts in the detector coordinates of individual observations. The spectrum is further adaptively binned to achieve a background-subtracted signal-to-noise ratio greater than 2.5.

We compare the positions of a few well identified X-ray sources with their optical counterparts (OB stars) and find no significant systematic offset ($\lesssim$ 0".5). Therefore, no astrometry correction was applied to the X-ray data. We caution however that these sources all lie at large off-axis angles, so that the uncertainties in their X-ray positions are large.

3. The catalog

The source detection algorithms found 165 sources in N11. Table 2 lists their positions, count rates and hardness ratios which can be used to characterize the X-ray spectral properties of the sources by comparing with spectral models (e.g., **?** WHICH WANG ET AL 2006?). The conversion from a count rate to an unabsorbed energy flux depends on the source spectrum and foreground absorption. A characteristic value of the conversion is 8×10^{-12} (erg cm^{-2} s^{-1})/(counts s^{-1}) in the 0.5–8 keV band for a power law spectrum of photon index 2 and an absorbing-gas column density $N_H \sim 1 \times 10^{21}$ cm^{-2} (assuming the solar abundances). This conversion should be a good approximation (within a factor of 2) for $\lesssim 3 \times 10^{21}$ cm^{-2}. The corresponding conversion to a source-frame luminosity in the same band is $\sim 2.4 \times 10^{36}$ (erg s^{-1})/(counts s^{-1}) at the LMC distance of 50 kpc.

Fig. 2 presents an overview of the ACIS-I 0.5–8 keV band image with the detected X-ray sources indicated, while Fig. 3 show a three-color map of the X-ray emission in N11. One may notice in Fig. 2 a few mis-matches between apparent peaks in the smoothed X-ray image and the detected sources. This is at least in part due to the different significance thresholds used in the source detection (based on Poisson statistics) and the image smoothing (Gaussian statistics). The significance in the Poisson statistics depends on the background level: a source with 5 counts, for example, may be detected as a source with $P < 10^{-6}$, if the background level is sufficiently low, but such a source alone will not meet the smoothing threshold of Gaussian $S/N \sim 3$. Conversely, a $S/N \sim 3$ peak may not satisfy the above source detection threshold if the background is high, typically in a large off-axis region.

3.1. Variability of the X-ray sources

We conduct tests for timing variability for sources with detected $S/N \gtrsim 4$ and not near CCD boundaries (with a 12" margin to account for the dithering effect). First, we carry out the Kolmogorov-Smirnov test based on individual observations in the three source detection bands. Only J045539.69−662959.5 shows an apparent variation in the S band during the observation #8210 and at a confidence level of $\sim 3\sigma$. This variability was confirmed by a χ^2 test (Fig. 4). Next, we use the entire date sets from the six observations for similar tests, but we restrict to sources that are not near the CCD gaps in any of the observations. Sources J045509.20−663018.5 and J045702.07−662257.1 (Fig. 4) show variabilities at the confidences of 5 and 3σ, respectively.

3.2. Number-flux relation of the X-ray sources

To characterize the X-ray source number-flux relation (NFR) in N11, we need to account for various complications involved in the source detection and the confusion with interlopers (foreground stars and background AGNs). For simplicity, our NFR analysis here uses only the 141 sources detected in the 0.5–8 keV band because sources detected only in the 2–8 keV band tend to be obscured AGNs, whereas those only in the 0.5–2 keV band are likely to be either foreground stars or diffuse X-ray emission peaks in the LMC.

The source detection completeness varies across the ACIS-I map, depending on the local

PSF, effective exposure, and background. The detection is also subject to the so-called X-ray Eddington bias: more intrinsically faint sources statistically appear to have higher fluxes than the other way around. We correct for both the incompleteness and bias in our NFR analysis, following the approach detailed in Wang (2004). Briefly, the NFR is analyzed as if it is an X-ray spectrum with the field-integrated incompleteness and flux bias included in the weighted effective area and response matrix.

Fig. 5 shows the differential NFR of the all selected sources and our modeling. We use the background source Log(N)–log(S) relation in the 0.5–2 keV band, as presented by Moretti et al. (2003, and references therein). However, the X-ray absorption through N11 ($N_H = 4.3 \times 10^{20}$ cm^{-2} plus the absorption in the LMC) is substantially higher than that toward the *Chandra* deep fields (foreground absorption 1.6×10^{20} cm^{-2}). We calculate the count rate dependence on the band choice and on the absorption, using XSPEC, assuming a power law spectrum of photon index of 1.4 (Moretti et al. 2003). For the pixel-by-pixel absorption correction, we use an HI map of the LMC with a spatial resolution of XXX (ATCA+PKS, YHC: REFERENCE NEEDED), assuming a metallicity of 30% solar. We find that the expected AGN contribution to our selected sources is ~ 91 (Fig. 5). We find that the residual (N11) contribution can be reasonably well fitted with a power-law

$$\left(\frac{dN}{dS}\right) = AS^{-\alpha}, \tag{1}$$

where S is in the 0.5–8 keV band and in units of counts s^{-1}, while $\alpha = 1.9^{+0.3}_{-0.2}$ and $A = 10^{-1.9^{+1.0}_{-1.1}}$ sources per arcmin^{-2} counts s^{-1} (error bars are all at the 90% confidence).

4. High-mass X-ray binaries

Shtykovskiy & Gilfanov (2005) analyzed *XMM-Newton* observations of the LMC with the purpose of finding HMXB candidates in the region surveyed. They defined selection criteria enabling to identify HMXBs candidates by cross-correlating the X-ray positions with optical and near-infrared catalogs. We apply these criteria to investigate whether HMXB candidates are present in the N11 field-of-view (FOV).

Our *Chandra* observations resulted in the detection of 165 point sources. Following Shtykovskiy & Gilfanov (2005), we used the following optical and near-infrared catalogs: USNO-B, version 1.0 (Monet et al. 2003); Guide Star Catalog, version 2.2.1 (Morrison et al. 2001); 2MASS (Cutri et al. 2003); DENIS (Cioni et al. 2000). We also cross-correlated X-ray sources with the Spitzer IR-sources reported in Hatano et al. (2006). The search radius 3.6″ was used to correlate the catalogs with our *Chandra* source list.

Excluding known massive stars (see below), we have found optical counterparts for 91 X-ray sources. To search for X-ray binaries, we then apply several selection criteria: $R < 17.5, R-I < 1.5, B-R < 1.5, V-R < 1.5, J-K > 0.7$, or $I-K > 0.7$ and exclusion of objects classified as "extended" in GSC 2.2.1. 87 objects were thus excluded. Among the remaining three sources, one was rejected because of its too low X-ray-to-optical flux that indicates that the object is a foreground star. For the two remaining objects, the X-ray-to-optical flux is lower than typically found in the confirmed X-ray binaries, $F_{\rm X}/F_{\rm opt} > 10^{-2}$. One of these two objects has a proper motion exceeding that of the LMC and can thus further be excluded, while the I color is not available for the second one. Therefore, we conclude that there are no HMXB candidates among the X-ray point sources detected in N11.

Since the *Chandra* FOV during our observation covered two young massive star clusters, LH 9 and LH 10, one may winder whether this non-detection is suprising or not. The stellar content of LH9 and LH10 was studied by Parker et al. (1992) using UBV photometry. They derive ages of 1–2 Myr and 3–4 Myr for LH9 and LH10, respectively. More recently, Mokiem et al. (2007) studied the optical spectra of a much smaller sample of OB stars (22 objects) but they used modern stellar atmosphere models. They derived larger values for the ages: 7.0 ± 1.0 Myr and 3.0 ± 1.0 Myr for LH 9 and LH 10 respectively. If we consider the latter values as the most accurate ones, the age of LH 9 is the most favorable for the production of HMXBs (Sepinsky et al. 2005; Clark et al. 2008).

For a 7 Myr old star cluster the observed mass-function does not fully represent the IMF because the most massive stars have already finished their lives. There are $\approx$ 180 stars with masses between $10\,M_\odot$ and $61\,M_\odot$ presently observed in LH 9 (Parker et al. 1992; Mokiem et al. 2007). Assuming that the IMF of the LH 9 is represented by a Salpeter law with upper cut-off at $150\,M_\odot$ and lower cut-off with $0.5\,M_\odot$, there must have been 12-14 stars more massive than $60\,M_\odot$. At 7 Myr of age these most massive stars have already underwent supernovae explosions. Under the same assumption, the total mass of LH 9 can be estimated to $M_{\rm LH\,9} \approx 6 \times 10^3\,M_\odot$. Recently, Clark et al. (2008) provided an empiric estimate of the X-ray binary fraction as a function of star cluster mass. From studies of star clusters in the Antenae galaxies and accounting for the differences in cluster ages they found that the fraction of X-ray sources per unit mass as a function of cluster mass is quite small, $\eta(M_{\rm cl}) = 1.7 \times 10^{-8}\,M_\odot^{-1}$. The lack of detected HMXB candidates in N11 is thus consistent with this estimate. It is however interesting to note that the low value of η in star clusters is in some apparent contradiction with the census of HMXBs in the Milky Way conducted by Helfand & Moran (2001). These authors found that within 3 kpc from the sun, 0.1%–0.2% of all the early-type stars are currently active accretion-powered X-ray sources.

5. Correlation with Spitzer data

6. Massive stars

6.1. The massive star population in the *Chandra* field

The two massive star clusters covered by our *Chandra* observation appear very different from one another. LH9 is the most extended and the richest cluster in N11. It is dominated by HD32228, a bright, compact OB group containing one Wolf-Rayet star of the carbon sequence (Brey 9) and at least 11 late O-type stars (Walborn et al. 1999). In contrast, the LH10 cluster, still partly embedded in its natal cloud, appears rather pristine. Its wind-blown bubbles are still of limited size (Nazé et al. 2001) and even the earliest O-type stars remained intact: LH10 actually contains no less than three examples of the rare O2-3 objects (Evans et al. 2006, hereafter ELST, and references therein), one of them belonging to the compact OB group PGMW 3209 (Walborn et al. 1999). The IMF in both clusters was constrained to $\Gamma_{\rm LH10} = -1.1 \pm 0.1 < \Gamma_{\rm LH9} = -1.6 \pm 0.1$ (Parker et al. 1992). This confirms that there are many more high-mass stars in LH10 than in LH9. These facts, together with the higher reddening of LH10, indicate the relative youth of LH10 compared to LH9 (about 2 Myr difference, see Parker et al. 1992; Mokiem et al. 2007). Because of the position of LH10 at the periphery of the LH9 superbubble, it was further suggested that the pair constitutes an example of sequential star formation (Walborn & Parker 1992).

Several spectroscopic and photometric studies of LH9 and LH10 have been performed. The first complete study was that of PGMW, which provided spectroscopic classification for about 75 stars, among which 43 O-type objects. Using HST data, Walborn et al. (1999) were able to disentangle the two compact OB groups HD32228 and PGMW3204/9 and they further investigated their stellar content. These authors give spectral classification for 20 additional hot stars. Recently, the VLT Flames Survey has re-observed the region, leading to the discovery of 25 new O-type stars (ELST[2]), including a potential runaway star of type O2.5III. In total, 1 Wolf-Rayet, 81 O-type stars and 80 B-type stars are now known in the *Chandra* FOV. The spectral monitoring of ELST further indicated a binary fraction of 36% in LH9-10. Finally, Mokiem et al. (2007) performed a detailed atmosphere modelling on 22 of the ELST targets, leading to the first accurate determination of their physical properties.

In the X-ray domain, N11 was previously observed by Rosat (Mac Low et al. 1998; Dunne et al. 2001) as well as by XMM-Newton (Nazé et al. 2004). However, the crude point-spread-function of these facilities did not lead to unambiguous detections of X-ray

[2]Note that 4 O and 9 B of ELST stars are out of the *Chandra* FOV.

emission associated with the OB stars of LH9 or LH10.

6.2. Detection of massive X-ray emitters in N11

At first sight (see Fig. 2), the X-ray point sources do not appear obviously clustered towards LH9, LH10 or their periphery. Indeed, correlating the list of X-ray sources (see Table 2) with the list of known OB stars led only to 14 positive matches. As some X-ray point sources were missed, especially when superimposed on strong diffuse background, we further inspected the X-ray image by eye. One additional X-ray source associated with an O-type star was then detected. It lies near a rather bright point source and on the edge of diffuse emission, which explains its non-detection by the search algorithms.

Table 3 lists the properties of these 15 OB stars with detected X-ray emission. The first eight columns report the X-ray source number, count rate and hardness ratio (from Table 2), the ELST or PGMW identification, the spectral type and binary status (from ELST, Walborn et al. 1999, or PGMW; C? indicating a possible composite spectrum). In addition, we derived for each object the color excesses E(B-V) from the BV photometry, using the intrinsic colors from Martins & Plez (2006). Galactic reddening towards the LMC was estimated to 0–0.15 mag by Oestreicher et al. (1995); as the reddening of some of our stars is $\sim$ 0, we will consider the Galactic contribution negligible and we therefore calculate the absorbing columns $N_{\rm H}$ using a gas-to-dust ratio of 2.4×10^{22} cm^{-2}, typical of the LMC (Fitzpatrick 1986). The bolometric luminosities, when not estimated by Mokiem et al. (2007), were also derived from the BV photometry with intrinsic colors and bolometric corrections from Martins & Plez 2006; they were derived using the properties of the earliest component if the object is SB2. The derived absorbing columns and bolometric luminosities are presented in the ninth and tenth columns of Table 3. The last two columns of that table give the unabsorbed flux (in the 0.5–10 keV band) and L_X/L_{BOL} ratio.

Six of the sources have enough counts (>80 cts) for a rough spectral analysis. They were modeled within XSPEC using an absorbed thermal model (XSPEC models mekal and vphabs, both with metal abundances set to 0.3 times solar). Results of these fits are shown in Table 4. Generally, because of the low statistics, two solutions of rather similar quality can be found: one with high T-low $N_{\rm H}$, the other with low T-high $N_{\rm H}$. Even for the latter, the temperature always exceeds 0.5 keV, which is rather high for single O-type stars (typipcal kT ~0.3 keV, see e.g. Sana et al. 2006). This high temperature combined to the large $L_X - L_{BOL}$ ratios of these objects might indicate that the sources actually are colliding-wind binaries or young magnetic (single) stars.

For the fainter sources, we derived fluxes from the count rates using XSPEC v 12.3.1 and the calculated absorbing column. Typical on-axis response matrices were used to transform the count rates into fluxes. The chosen model was a thermal one with a temperature kT=0.3 keV (typical for O-type stars, e.g. Sana et al. 2006) absorbed by the $N_{\rm H}$ determined above (XSPEC models mekal and vphabs, both with metal abundances set to 0.3 times solar). The derived conversion factor between count rate (in cts ks^{-1}) and unabsorbed flux (in erg cm^{-2} s^{-1}) was 0.6–3$\times 10^{-14}$, depending on the absorbing column.

Only two of the detected sources are B-type stars, the detection fraction for these objects is thus $\sim$2.5% (2 out of 80). This is not surprising since B-type stars are generally not bright X-ray emitters and X-ray emission apparently associated with such objects has generally been attributed to a flaring PMS companion (see e.g. Sana et al. 2006) or to an accreting compact companion. In N11, though, the two B stars detected present very early types (B0-B0.2) and their emission could thus at first be considered as the low-luminosity tail of the $L_X - L_{BOL}$ relation for O-type stars. While this could be true for ELST33, whose count rate is accordingly low (2σ detection), it is not the case for ELST163. This is one of the brightest X-ray point sources associated with OB stars (see Table 3). The remaining possibilities, compatible with the high HR of the source and its hard spectrum (see Table 4), are thus a line-of-sight coincidence or a PMS/compact companion. In this context, it might be worth noting that the star was found to be a binary, but was not classified as a Be object (ELST).

Most of the detected sources correspond to hot, O-type objects. Two of them correspond to the compact OB groups HD32228 and PGMW3204/9, while another one is associated with the compact HII region N11A and its small cluster (see individual discussion for these below). Amongst the 10 remaining O-type objects, only 2 are known binaries, i.e. a fraction of 20%, a value slightly lower than the binary fraction of the clusters (36%, ELST). This would suggest that O-type binaries were not preferentially detected in N11. This surprising result contrasts with what happens in the Galaxy (O+O or WR+O binaries being generally brighter than single objects because of the possible additional contribution of colliding winds to the high-energy emission). We caution however that the monitoring of ELST was limited and that binary systems might have been missed.

Overall, the fraction of detected O-type stars is 16% (10 out of 62), excluding the 19 stars in compact groups (N11A, PGMW3204/9, HD32228). When ranked by magnitude or spectral types, it appears that the hottest and/or earliest objects are preferentially detected, as could be expected (70% of the detected sources belong to the brighter half of the O-type list; the detection fraction is 57% for early, O2–5 stars, 25% for mid, O5.5–O7 stars and 3% for late, O7.5–9.7 stars). Of the four O2–3 stars present in the field, only two are detected:

the one belonging to the PGMW3204/9 compound and ELST31. These are not known binaries, nor are they necessarily the brightest earliest-type stars (ELST26 being slightly brighter than ELST31). However, the L_X/L_{BOL} ratio of ELST31 is quite large and there are additional stars in the PGMW3204/9 compound (see Table3), suggesting that there exists an additional source of X-rays than the simple intrinsic emission of an O2-3 star.

To gain further insight onto the global properties of the OB star population, we estimated the count rates of all OB sources in the field using their catalogued positions and corresponding 90% EER. From these measurements, we adopted the 1σ error as an upper limit on the count rate for each undetected OB object. These upper limits on the count rates were transformed into upper limits on the unabsorbed flux as was done above for the fainter detected sources. Note that while the lowest count rate of detected sources is $\sim 0.05\mathrm{cts\,ks^{-1}}$, the undetected OB stars only emits about 0.7 ± 0.6 cts ks^{-1} taken all together.

Table 5 summarizes the properties of these undetected O-type stars present in the *Chandra* FOV. Columns one and two give the star number in ELST and PGMW, respectively; the third and fourth column indicate the spectral type and binary status; the fifth column provides the bolometric luminosity as given by Mokiem et al. (2007) when available or as derived from the BV photometry otherwise; the sixth column lists the absorbing columns, derived from the photometry as explained above; the last columns yield the upper limits on the X-ray luminosity and on the L_X/L_{BOL} ratio.

Fig. 8 presents the full results in a graphical way. Except for the HD32228 compound, all detected sources clearly lie above the Galactic $L_X - L_{BOL}$ relation. If these objects truly represents typical examples of O-type stars, the inferred $L_X - L_{BOL}$ relation lies ~0.5 dex higher, i.e. the O stars would be about 0.5dex, or a factor of 3, brighter in the X-ray domain in the LMC compared to the Galaxy. While a brighter $L_X - L_{BOL}$ relation would generally agree with the upper limits derived, it contradicts a priori intuitions (lower metallicity→weaker winds→fainter X-ray emission). However, the detected objects display large hardness ratios and temperatures and they are thus potential wind-wind interacting systems or peculiar magnetic objects. They might therefore not be fully representative of the properties of the O-type population in N11. Further study should be undertaken to clarify the status of the detected objects ('typical' single stars, colliding-wind binaries, young magnetic objects?) before drawing any firm conclusion on the actual $L_X - L_{BOL}$ relation in the LMC.

6.3. Individual objects

6.3.1. HD32228 and its environment

The main component of LH9, the compact group also known as HD32228, is clearly detected in our observations (Fig. 6). Its X-ray emission follow the visible one, i.e. it is not a simple point source and looks rather extended. The morphology is actually reminiscent of a point-like source superimposed on a small region of diffuse emission, itself immersed in the fainter superbubble emission from the whole cluster. We have extracted spectra of each of these 3 regions (see Tables 4 and 6).

The emission peaks at the position of the Wolf-Rayet component, Brey 9 or BAT99-10. Since this evolved object belongs to the carbon sequence, it is not expected to emit significant amounts of X-rays if single (Oskinova et al. 2003). The total luminosity from all O-type stars in the HD32228 compound amounts to $\sim 7.5 \times 10^{39}\mathrm{erg\,s^{-1}}$, implying a $\log(L_X/L_{BOL})$ ratio of -7.1 ± 0.1, fully compatible with the Galactic value.

The surrounding area ('near HD32228', see Table 6), once cleaned of the superbubble 'background' contribution, presents a harder spectrum than the emission associated with the superbubble itself. Its high temperature and high absorption suggests the emission to be dominated by the overall X-rays from unresolved stellar objects, most probably O and PMS. On the contrary, another region in LH9 with higher surface brightness ('inside LH9', see Table 6) displays a spectrum very similar to the superbubble itself - only a few deviant high-energy bins, maybe spurious, are detected as a very high temperature plasma with low EM. To the limits of our data, the X-ray emission associated with LH9 thus appears rather uniform if one excludes HD32228 and its surroundings.

6.3.2. LH10

Fig. 7 shows a close-up on the LH10 cluster. In this region, six point-like sources are detected. They correspond to five O-type stars (ELST 31, 38, and 50, PGMW 3070 and 3120) and one compact group (PGMW3204/9). The brightest source, PGMW3070, appears actually as a tight cluster in the HST images. The point-like source associated with the two subclusters display a slightly elongated shape, probably indicating that they are not truly point-like sources. Their flux is also too high for a single star, with $\log(L_X/L_{BOL})$ of -6.0 for the sole PGMW3070. The ratio appear to have a more reasonable value of -6.8 ± 0.1 for PGMW3204/9 but this happens only if we consider the sum of the individual luminosities of this stellar group's components. The flux of the other sources in LH10 is also higher than expected for Galactic single O-type stars. This is especially the case of the bright binary ELST50, which presents the highest $\log(L_X/L_{BOL})$ ratio: even taking into account the presence of two stars, the X-ray source is still about 5 times brighter than expected. Again, colliding winds might be the source of additional X-rays in binaries, and a magnetically-confined disk could play a similar role for the single objects. It is also interesting to note that in our data, PGMW3204/9 appears nearly as bright as PGMW3070, whereas it seemed much fainter during the XMM observations (compare our Fig. 7 with Fig. 11 of Nazé et al. 2004): this may indicate some variability in its high-energy emission, which is generally associated with an orbital or rotational modulation.

Some diffuse emission is also present throughout the field, especially to the southwest of the cluster, near PGMW 3070 and 3120. In this region, a wind-blown bubble was detected by Nazé et al. (2001). However, another expanding bubble was found east of PGMW 3204/9 and ELST 50, with similar expansion velocity but it does not appear to be associated with diffuse emission as bright as the former. Higher velocity structures were also detected, but appear to the south and west of the X-ray bright region. It might be noted that the diffuse emission, which appears centrally peaked rather than bright-rimmed, corresponds to the region of highest stellar density - the eastern part of LH10 being much less crowded. This could suggest that at least part of the X-ray emission actually comes from unresolved stars. This hypothesis seems confirmed when the spectrum of that diffuse emission is analyzed (Table 6): two thermal components are present, one with a low temperature typical of soft diffuse emission and one with a high temperature, most probably stellar in origin.

6.3.3. N11A

The compact HII region N11A, lying to the east of LH10, probably harbors the youngest optically-visible stars in the field (Heydari-Malayeri et al. 2001). It is associated with the 'star' PGMW3264 or ELST28, which is actually the earliest component of a compact stellar group composed of 7 objects. The associated X-ray emission is rather strong and a comparison of its shape with that of its neighbours suggests some extension. Since the earliest object was repeatedly proposed to be a mid O-type star (Heydari-Malayeri et al. 2001; Evans et al. 2006) and because of the high extinction, strong X-ray emission from single stars is not expected. The X-ray emission could thus be associated with wind-wind interactions between the cluster members or the addition of several unresolved sources (young magnetic objects or colliding wind binary systems). Unfortunately, the spectrum of this source is difficult to extract since it lies on the edge of some datasets. The crude X-ray spectrum only points to a high temperature, thus favoring the second interpretation, but the noise prevents us to draw clear conclusions. These results should therefore be taken with caution (especially since a low absorbing column is also favored by the noisy data, a fact clearly at odds with strongly extinguished sources within a dense blob).

7. Diffuse emissions: preliminary results

As can be seen in the color map of Fig. 3, soft diffuse emission pervades the *Chandra* FOV. On the basis of the luminosity, we defined 8 regions to be further analyzed (see Fig. 9 and Table 6 for their positions). Three regions displaying lower emission were chosen as backgrounds[3]. Spectra of these regions were extracted, taking into account the non-X-ray background (see Sect. 2) and excluding the regions surrounding the X-ray point sources detected in these areas. Although the work was done with care, the bins at very low (<0.3 keV) and very high energies (>2 keV) appeared rather noisy and had to be discarded.

To take into account the variations of the sensitivity across the FOV, we did not make the usual, simple background subtraction and the spectral fitting was thus done in two steps. First, each background and combination of background was fitted independently by a model of the form wabs*mekal+wabs*pow. The sources were then fitted by models of the form vphabs*mekal+wabs*mekal+wabs*pow, where the first component represents the true spectrum of the diffuse source (metal abundances of the absorption and thermal emission models were accordingly fixed to 0.3) and the last two represent the background (these were fixed to the best-fit background model with the normalisation factors scaled by the surface ratio). Second, the best-fit parameters found previously were used as first guess for a simultaneous fit of the diffuse source and its associated background. This time, no parameter was fixed, in order to improve the fit further. The results of these fits are presented in Table 6. The spectral analysis of two additional regions of LH9 that display a larger surface brightness are also presented in this table.

The spectra display a thermal component at low temperature ($kT \sim$0.2 keV). For LH9 and LH10, an additional plasma component was needed to obtain a good fit. The temperature of this second component is high, thereby suggesting it to be associated with unresolved stellar objects (PMS, O stars). This contamination is not negligible since it represents about one-third of the total flux associated with the diffuse sources. Its stellar origin is confirmed by analyzing the spectrum of the region (called 'middle') situated between LH9–LH10 and the northern limit of the FOV. The latter spectrum does not request the presence of a high

[3]Circles centered on (04:55:29.9,-66:18:19.7), (04:55:23.3,-66:29:38.6) and (04:55:48.8,-66:25:11.6) with radii 66.″3, 60.″7 and 54.″1, respectively

temperature component: indeed, only a few stars are scattered across this region and the stellar contribution is thus expected to be negligible. Note that a fit of the LH9 spectrum where the abundance of the low-temperature component is let free to vary does not improve the χ^2: to the limit of our observations, no significant modification of the abundances is thus detected.

The high absorbing columns of the regions situated to the east and west of LH9 might in fact be an artefact: if we use only one component to fit the spectra of LH9 or LH10, the best-fit also yields a high absorption for these objects. Unfortunately, the spectra of these two diffuse sources are too noisy for making a meaningful $2T$ fit. Keeping this caveat in mind, one can however see the remarkable homogeneity of the derived spectral parameters, e.g. the similar confidence intervals for the temperature and the absorbing columns for the $1T$ fits. Only the region above LH9 presents some significant absorption, which is unsurprising because of the presence in this area of dust lanes.

8. Summary and conclusions

This paper report the first results of a very deep *Chandra* observation of the giant HII region N11 in the LMC. Thanks to the long exposure (300 ks) and the high spatial resolution, 165 X-ray point-sources were detected in the field, with all but 3 showing no significant temporal variability. Our *Chandra* observation thus multiply by more than five the number of point-sources known in N11. Keeping in mind that the sensitivity varies across the field, it must be noted that the faintest detected sources have count rates of about 0.05 cts ks^{-1}, which correspond to luminosities of about 10^{32} erg s^{-1}.

Most of the X-ray sources are background objects seen through the LMC. Moreover, there is no X-ray binary in the field, as expected by the young age of most clusters and the low mass of the oldest one. However, 15 OB stars are clearly detected in X-rays, three of them corresponding to compact clusters (HD32228, PGMW3204/9, and N11A). Contrary to what happens in the Galaxy, the known binaries seem not preferentially detected in N11, though this conclusion might be biased by the incomplete knowledge of the stellar multiplicity. If the detected objects are truly representative of the massive star population, then the intrinsic X-ray emission would be brighter in N11. Alternatively, these stars could correspond to interacting winds systems or magnetic objects, as may be suggested by their rather high plasma temperatures. Follow-up observations are therefore needed to ascertain the nature of these sources.

YN acknowledges support from the Fonds National de la Recherche Scientifique (FRS-

FNRS, Belgium), the University of Liège, The University of Illinois at Urbana-Champaign, and the PRODEX XMM and Integral contracts.

Facilities: CXO (ACIS).

REFERENCES

Barbá, R. H., Rubio, M., Roth, M. R., & García, J. 2003, AJ, 125, 1940

Cioni, M.-R., et al. 2000, A&AS, 144, 235

Clark, D. M., Eikenberry, S. S., Brandl, B. R., Wilson, J. C., Carson, J. C., Henderson, C. P., Hayward, T. L., et al., 2008, ApJ, 678, 798

Cutri, R. M., Skrutskie, M. F., van Dyk, S., et al. 2003, yCat, 2246

Dunne, B. C., Points, S. D., Chu, Y.-H. 2001, ApJS, 136, 119

Evans, C. J., Lennon, D. J., Smartt, S. J., Trundle, C. 2006, A&A, 456, 623 (ELST)

Feigelson, E., et al. 2002, ApJ, 574, 258

Fitzpatrick, E. L. 1986, AJ, 92, 1068

Hatano, H., et al. 2006, AJ, 132, 2653

Helfand, D. J., & Moran, E. C. 2001, ApJ, 554, 27

Heydari-Malayeri, M., Charmandaris, V., Deharveng, L., Rosa, M. R., Schaerer, D., Zinnecker, H. 2001,A&A, 372, 527

Lucke, P. B., Hodge, P. W. 1970, AJ, 75, 171

Mac Low, M.-M., Chang, T. H., Chu, Y.-H., et al. 1998, ApJ, 493, 260

Martins, F., Plez, B. 2006, A&A, 457, 637

Mokiem, M. R., de Koter, A., Evans, C. J., et al. 2007, A&A, 465, 1003

Monet, D. G., Levine, S. E., Canzian, B., et al. 2003, AJ, 125, 984

Moretti, A., Campana, S., Lazzati, D., & Tagliaferri, G. 2003, ApJ, 588, 696

Morrison, J. E., McLean, B., GSC-Catalog Construction Team, II 2001, DDA, 32.0603

Parker J. W., Garmany C. D., Massey P., Walborn N. R., 1992, AJ, 102, 1205

Nazé, Y., Chu, Y.-H., Points, S. D., et al. 2001, AJ, 122, 921

Nazé, Y., Antokhin, I. I., Rauw, G., Chu, Y.-H., Gosset, E., Vreux, J.-M. 2004, A&A, 418, 841

Oestreicher, M. O., Gochermann, J., Schmidt-Kaler, T. 1995, A&AS, 112, 495

Oskinova, L. M., Ignace, R., Hamann, W.-R., Pollock, A. M. T., Brown, J. C. 2003, A&A, 402, 755

Rosado, M., Laval, A., Le Coarer, E., Georgelin, Y. P., Amram, P., Marcelin, M., Goldes, G., Gach, J. L. 1996, A&A, 308, 588

Sana, H., Rauw, G., Nazé, Y., Gosset, E., Vreux, J.-M. 2006, MNRAS, 372, 661

Sepinsky, J., Kalogera, V., & Belczynski, K. 2005, ApJ, 621, L37

Shtykovskiy P., Gilfanov M., 2005, A&A, 431, 597

Walborn, N. R., Drissen, L., Parker, J. W., Saha, A., MacKenty, J. W., White, R. L. 1999, AJ, 118, 1684

Walborn, N. R., Parker, J. W. 1992, ApJ, 399, L87

Wang, Q. D., 2004, ApJ, 612, 159

Wang, Q. D., Owen, F., & Ledlow, M. 2004, ApJ, 611, 821

This preprint was prepared with the AAS LaTeX macros v5.2.

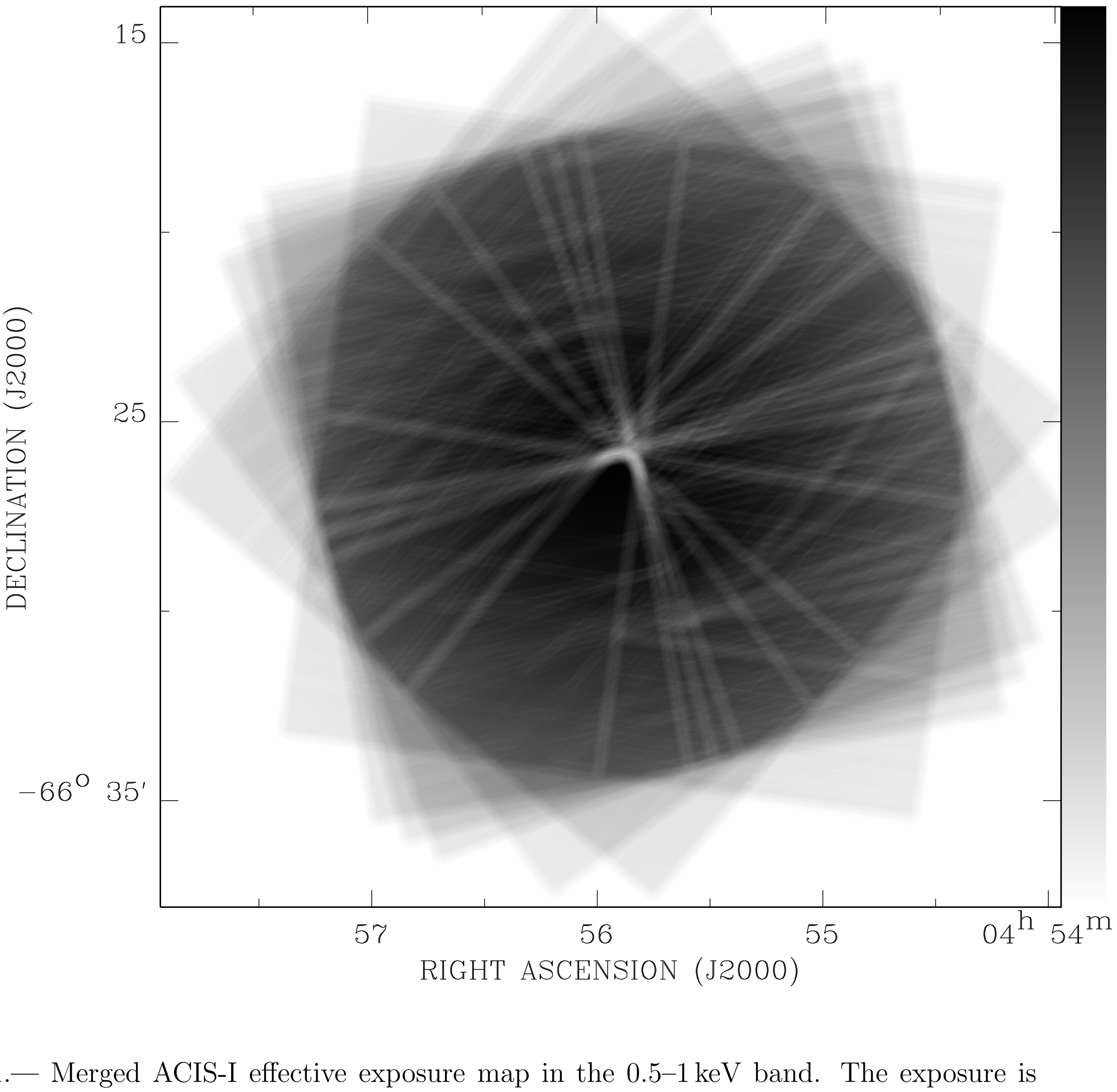

Fig. 1.— Merged ACIS-I effective exposure map in the 0.5–1 keV band. The exposure is linearly scaled in gray.

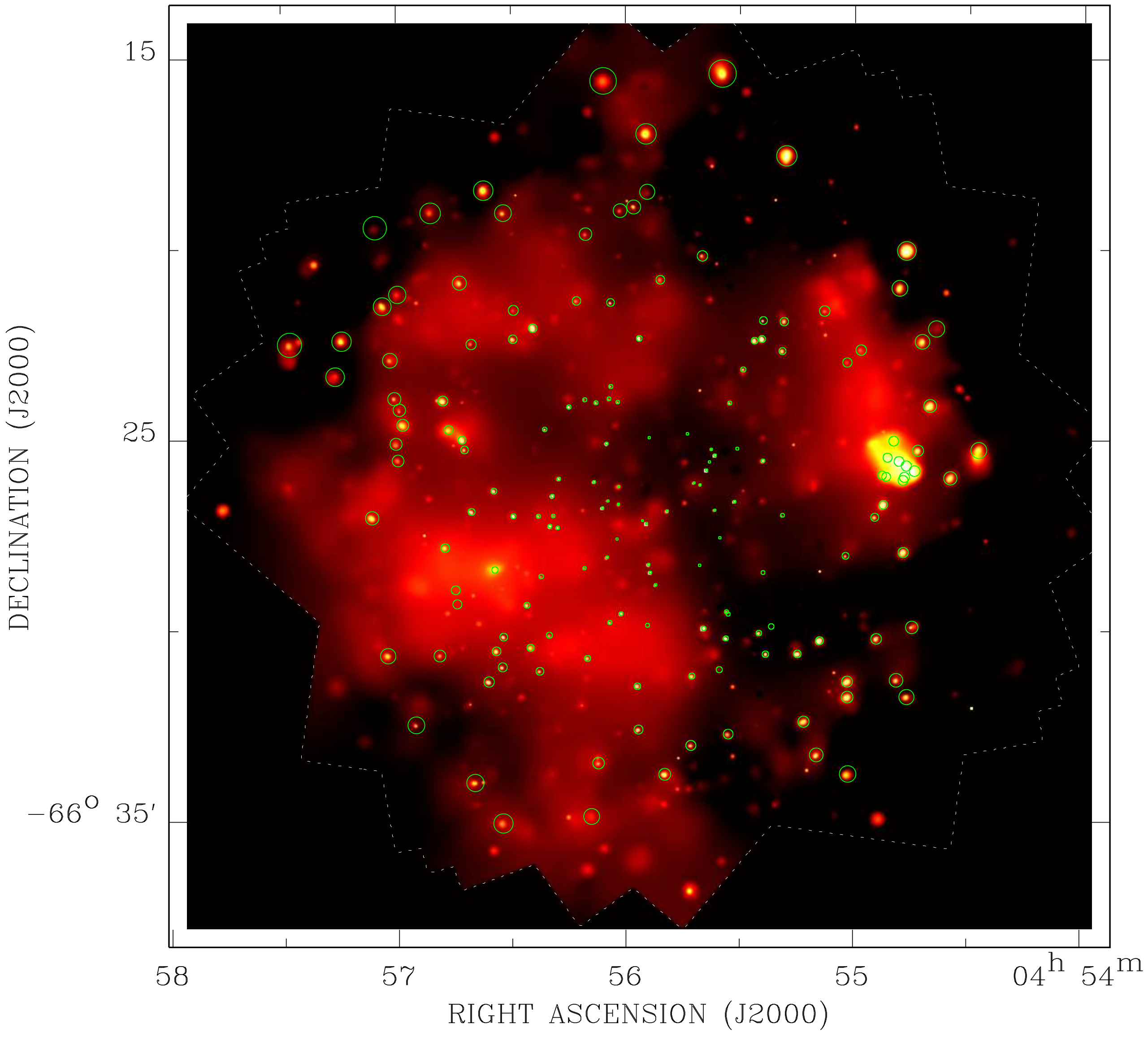

Fig. 2.— ACIS-I intensity image of N11 in the 0.5–8 keV band and detected sources (Table 2). The images are adaptively smoothed with the CIAO routine CSMOOTH. The smoothing scales are calculated separately in the 0.5–2 keV and 2–8 keV bands and with the S/N ratio ~ 3; the subtracted background is estimated locally in CSMOOTH. The circles illustrate the source removal regions of individual sources (see text for details). The white contours make the boundaries of the merged ACIS FoV (Fig. 1).

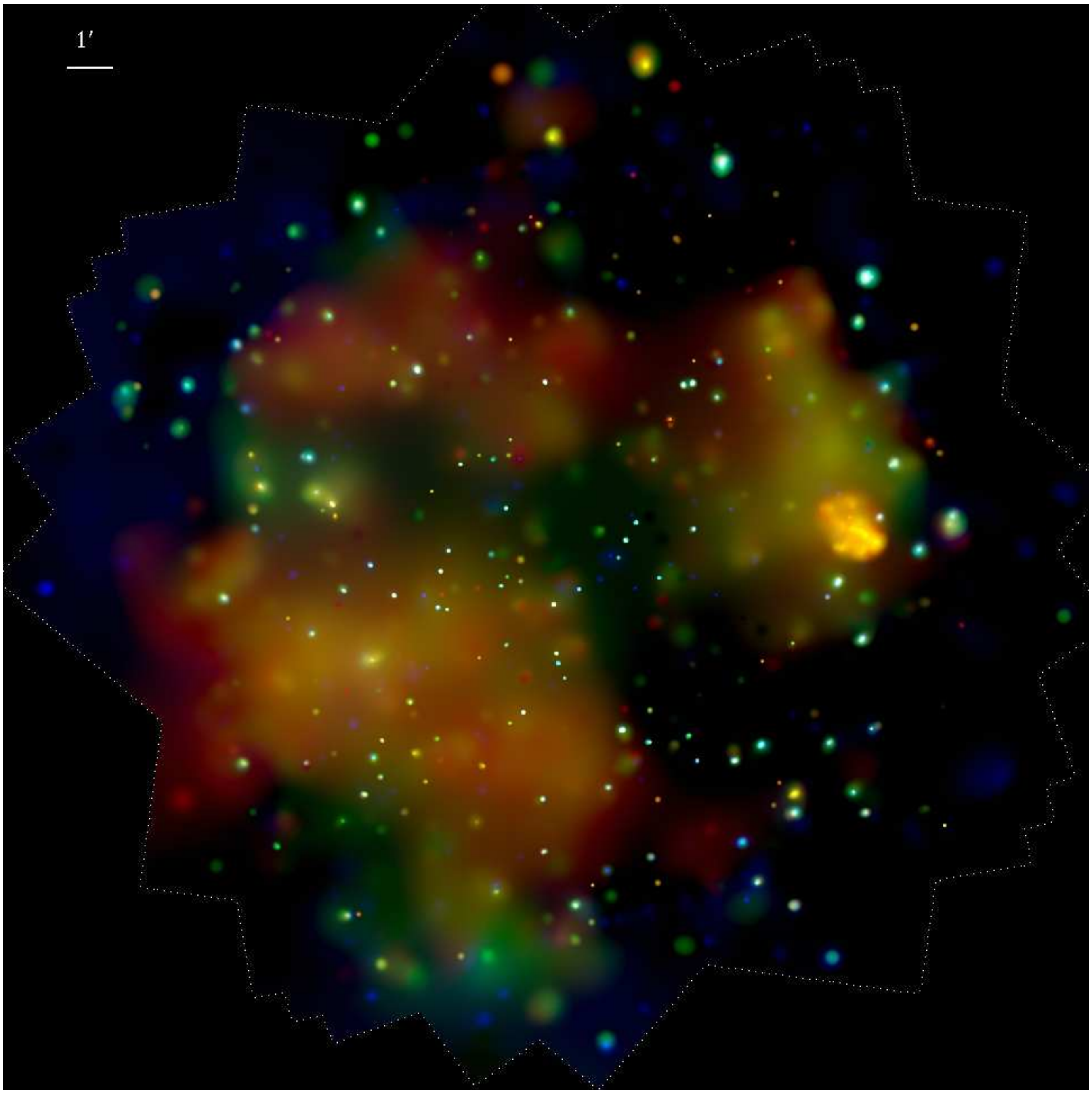

Fig. 3.— Tri-color montage of X-ray intensities: (red) 0.5–2 keV, (green) 2–4 keV, and (blue) 4–8 keV.

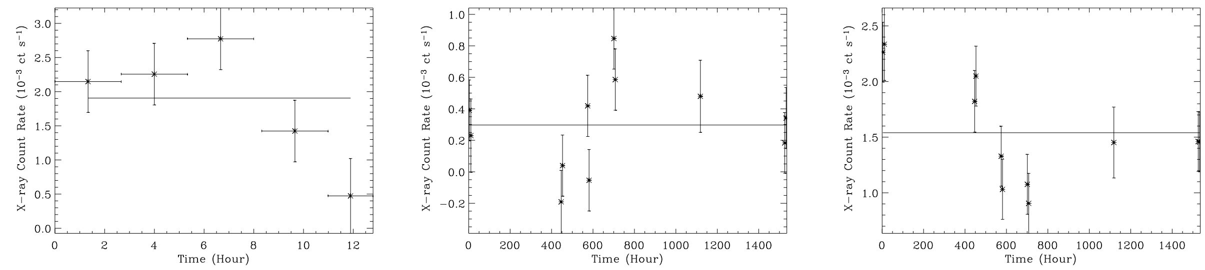

Fig. 4.— Illustrations of timing variability of three sources: J045539.69−662959.5 (left panel) during one observation; J045509.20−663018.5 (middle) and J045702.07−662257.1 (right) across the entire data set. The average count rates of individual sources are plottedas the horizontal straight lines.

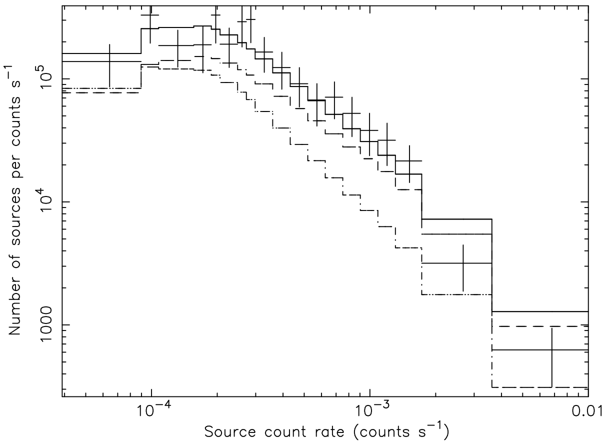

Fig. 5.— Observed differential NFR of the sources best-detected in the 0.5–8 keV band, compared with the best-fit power-law model. The data are grouped to have a minimum six sources per bin; the fit uses the Cash-statistic and is satisfactory, judged from simulations in XSPEC. The extragalactic AGN component is represented by the dashed histogram, while the power law component is by the dash-dotted one.

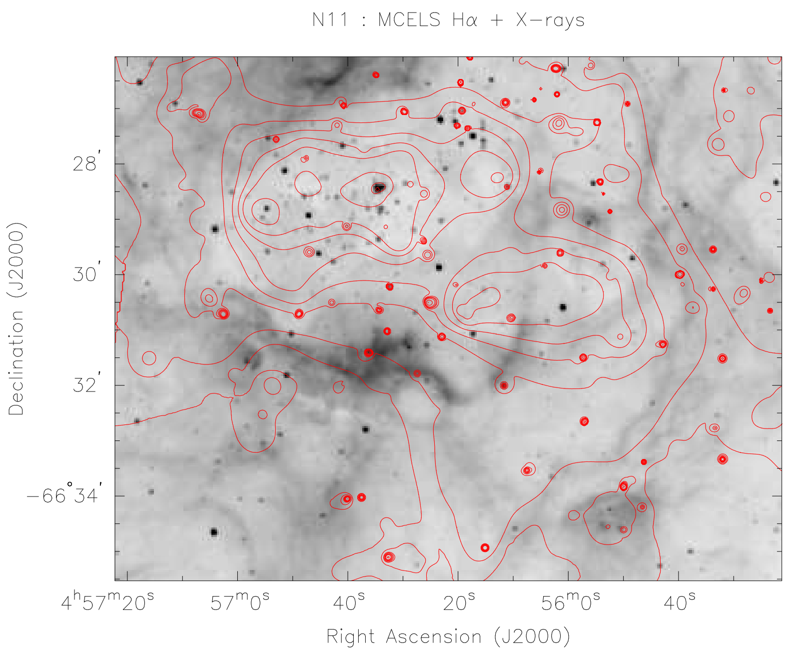

Fig. 6.— Hα image from the MCELS with X-ray contours superimposed. The adaptively smoothed X-ray image has been used here, and the contours are set at levels of 0.8,1,1.5,1.75,2,2.25,2.5,3,5,10,50 cts ks^{-1} arcmin^{-2}.

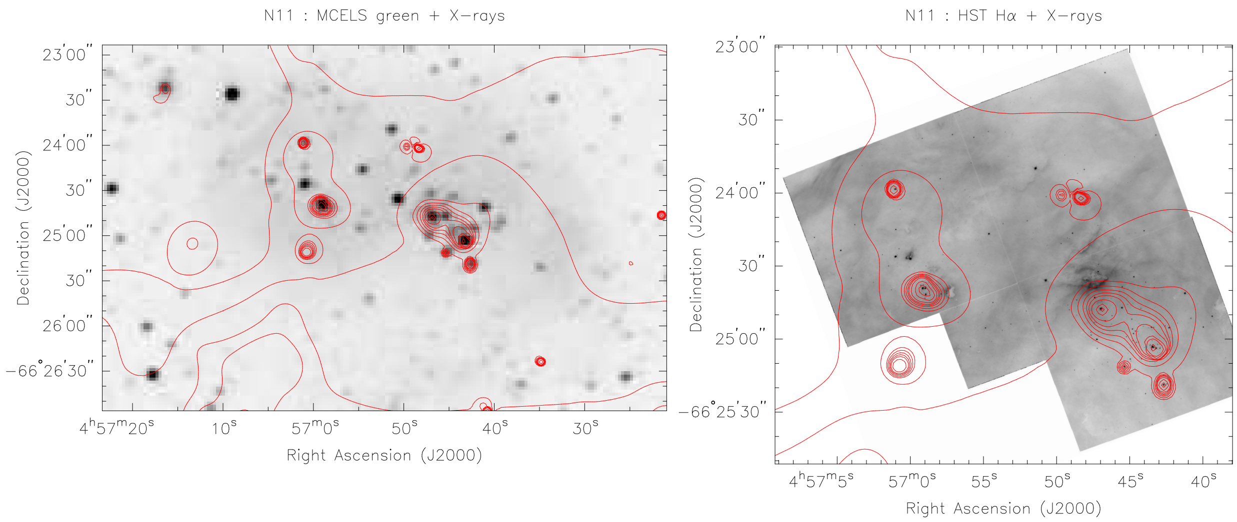

Fig. 7.— Two close-up on LH10. MCELS green image (left) or HST Hα image (Nazé et al. 2001, right, from) with X-ray contours superimposed (same as in Fig. 6).

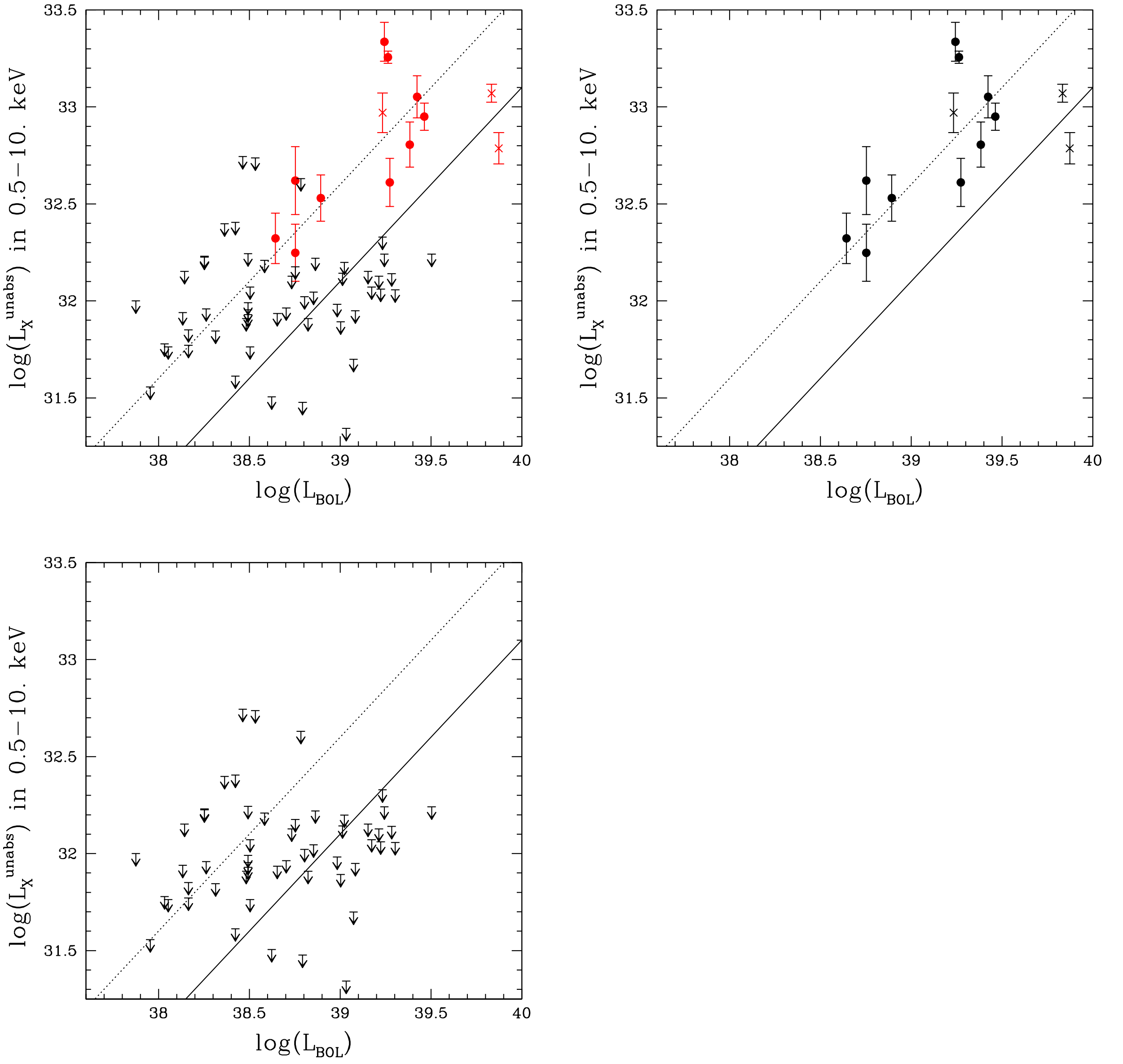

Fig. 8.— $L_X - L_{BOL}$ relation for O-type stars in the LMC as derived from the *Chandra* data. The three asterisks and the ten filled circles correspond to the compact groups and other detected O stars, respectively (see Table 3 for details), whereas the arrows give the upper limits on the X-ray luminosity for the undetected objects (see Table 5 for details). The solid line indicates the $L_X - L_{BOL}$ relation derived by Sana et al. (2006), the dotted line is 0.5 dex upper.

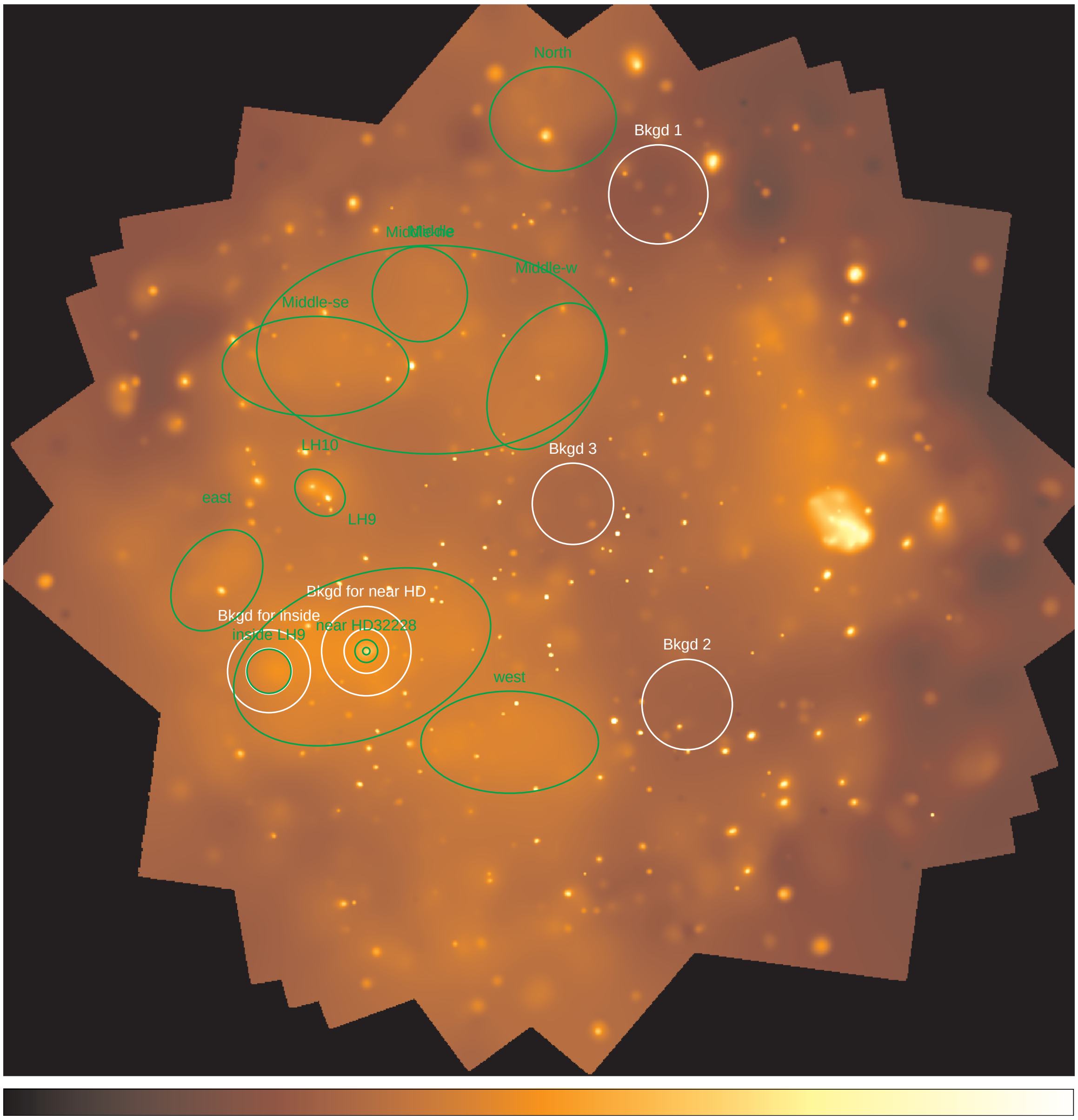

Fig. 9.— Definition of the extraction regions for diffuse emission (see Table 6 for their analysis).

Table 1: *Chandra* ACIS-I Observations[a]

OBS. #	R.A. (J2000) (h m s)	Dec. (J2000) (° ′ ″)	Exp (s)	Roll Ang (°)	OBS Date (yyyy-mm-dd)
8211	04 55 50.9	-66 26 14	47359	130.2	2007-07-31
8467	04 55 50.2	-66 26 29	48383	160.1	2007-06-27
8468	04 55 50.2	-66 26 31	47359	165.1	2007-06-22
8469	04 55 50.2	-66 26 34	48895	170.1	2007-06-17
8470	04 55 50.4	-66 26 21	42492	143.8	2007-07-14
8210	04 55 50.6	-66 26 42	45486	187.7	2007-05-29

[a] The exposure represents the live time (dead time corrected) of cleaned data.

Table 2. *Chandra* Source List

Source (1)	CXOU Name (2)	δ_x ($''$) (3)	CR (cts ks^{-1}) (4)	HR (5)	HR1 (6)	Flag (7)
1	J045427.48-662518.0	1.8	1.05 ± 0.10	-0.17 ± 0.13	0.53 ± 0.13	B, S, H
2	J045434.92-662602.1	1.5	1.16 ± 0.10	0.02 ± 0.10	0.89 ± 0.10	B, S, H
3	J045438.74-662207.1	2.4	0.21 ± 0.06	–	–	B
4	J045440.30-662408.4	1.5	1.72 ± 0.13	-0.39 ± 0.09	0.52 ± 0.09	B, S, H
5	J045442.40-662227.4	1.7	1.00 ± 0.09	0.25 ± 0.10	0.82 ± 0.15	B, H, S
6	J045443.47-662518.9	1.3	0.66 ± 0.08	0.08 ± 0.14	0.36 ± 0.18	B, S, H
7	J045444.36-662551.0	1.2	1.83 ± 0.15	-0.99 ± 0.15	-0.53 ± 0.06	S, B
8	J045444.89-662957.1	1.6	0.41 ± 0.07	0.34 ± 0.17	–	B, H, S
9	J045446.22-663146.7	1.9	0.77 ± 0.12	–	0.26 ± 0.19	B, S, H
10	J045446.51-662543.0	1.2	1.29 ± 0.13	-1.00 ± 0.15	-0.43 ± 0.08	S, B
11	J045446.60-662004.4	2.1	6.36 ± 0.28	-0.19 ± 0.05	0.60 ± 0.05	B, S, H
12	J045447.01-662600.9	1.2	0.52 ± 0.11	–	-0.66 ± 0.12	S, B
13	J045447.23-662759.2	1.1	1.62 ± 0.11	-0.12 ± 0.09	0.61 ± 0.09	B, S, H
14	J045447.36-662605.7	1.2	0.49 ± 0.09	–	-0.56 ± 0.13	B
15	J045448.38-662103.3	1.8	1.19 ± 0.11	-0.19 ± 0.11	0.72 ± 0.10	B, S, H
16	J045448.45-662535.9	1.1	1.04 ± 0.13	–	-0.74 ± 0.07	S, B
17	J045449.00-663120.4	1.7	0.53 ± 0.09	-0.06 ± 0.20	–	B, S, H
18	J045449.85-662504.9	1.3	0.27 ± 0.07	–	–	B, S
19	J045451.45-662530.0	1.1	0.65 ± 0.10	–	-0.94 ± 0.08	S, B
20	J045451.80-662600.1	1.1	0.38 ± 0.08	–	-0.44 ± 0.17	S, B
21	J045452.49-662644.3	1.0	3.36 ± 0.17	-0.23 ± 0.06	0.64 ± 0.06	B, S, H
22	J045452.85-662557.8	1.1	0.26 ± 0.06	–	-0.50 ± 0.19	S
23	J045454.26-663015.4	1.3	0.64 ± 0.07	-0.10 ± 0.14	0.76 ± 0.14	B, S, H
24	J045454.76-662704.0	1.0	0.28 ± 0.05	0.36 ± 0.20	–	B, H, S
25	J045458.44-662240.8	1.5	0.23 ± 0.05	–	–	B
26	J045501.67-663348.1	2.3	1.20 ± 0.27	–	–	B, S
27	J045501.86-663147.2	1.3	1.50 ± 0.11	-0.05 ± 0.09	0.58 ± 0.10	B, S, H
28	J045501.90-663122.8	1.2	1.68 ± 0.14	-0.76 ± 0.13	-0.22 ± 0.08	S, B
29	J045502.08-662300.4	1.4	0.10 ± 0.04	–	–	H, B
30	J045502.41-662804.8	1.0	0.13 ± 0.04	–	–	B
31	J045508.06-662139.6	1.5	0.20 ± 0.05	–	–	B, S
32	J045509.20-663018.5	0.9	2.52 ± 0.13	0.21 ± 0.06	0.88 ± 0.05	B, H, S
33	J045509.97-663318.3	1.8	0.47 ± 0.09	–	–	S, B
34	J045513.36-663226.1	1.3	0.89 ± 0.08	0.53 ± 0.09	–	B, H, S
35	J045515.02-663039.3	0.9	1.10 ± 0.09	-0.03 ± 0.10	0.53 ± 0.11	B, S, H
36	J045518.07-661735.4	2.3	5.06 ± 0.25	-0.13 ± 0.06	0.54 ± 0.07	B, S, H

Table 2—Continued

Source (1)	CXOU Name (2)	δ_x ($''$) (3)	CR (cts ks^{-1}) (4)	HR (5)	HR1 (6)	Flag (7)
37	J045518.65-662156.3	1.1	0.31 ± 0.05	0.16 ± 0.18	–	B, H, S
38	J045519.02-662701.2	0.6	0.10 ± 0.03	–	–	B, H
39	J045519.11-662242.7	0.9	0.30 ± 0.05	0.25 ± 0.18	–	B, H, S
40	J045521.93-662956.2	1.1	0.10 ± 0.04	–	–	S
41	J045523.45-663040.9	0.9	0.23 ± 0.04	–	–	B, S, H
42	J045524.11-662154.7	1.5	0.11 ± 0.04	–	–	S
43	J045524.12-662831.4	0.8	0.08 ± 0.02	–	–	B
44	J045524.13-662535.5	0.4	0.44 ± 0.05	-0.02 ± 0.15	0.72 ± 0.14	B, S, H
45	J045524.46-662223.8	0.8	1.75 ± 0.11	-0.25 ± 0.07	0.77 ± 0.06	B, S, H
46	J045525.18-663006.6	0.7	0.26 ± 0.05	–	0.76 ± 0.17	B, S
47	J045526.41-662226.4	0.8	0.83 ± 0.08	-0.14 ± 0.12	0.62 ± 0.11	B, S, H
48	J045529.39-662311.8	0.8	0.15 ± 0.04	–	–	B, S
49	J045530.93-662516.4	0.5	0.10 ± 0.03	–	–	B, S
50	J045531.60-662639.7	0.3	0.36 ± 0.05	0.48 ± 0.13	–	B, H, S
51	J045532.90-662404.6	0.6	0.14 ± 0.03	–	–	B, S, H
52	J045533.23-663245.8	1.3	0.31 ± 0.06	–	–	B, H, S
53	J045533.29-662936.9	0.8	0.07 ± 0.02	–	–	B
54	J045533.70-662933.3	0.6	0.11 ± 0.03	–	–	B, S
55	J045533.84-663015.2	0.6	0.70 ± 0.08	-0.12 ± 0.13	0.97 ± 0.06	B, S, H
56	J045534.88-661526.0	3.6	2.26 ± 0.51	–	-0.21 ± 0.18	S, B
57	J045535.48-662736.7	0.7	0.06 ± 0.02	–	–	B, S
58	J045535.59-663104.3	1.1	0.12 ± 0.04	–	–	H
59	J045536.75-662526.8	0.3	0.80 ± 0.08	-0.06 ± 0.12	0.95 ± 0.06	B, H, S
60	J045536.79-662653.3	0.5	0.08 ± 0.02	–	–	B, H
61	J045537.76-662517.7	0.5	0.08 ± 0.02	1.00 ± 0.01	–	H, B
62	J045538.24-662537.3	0.7	0.05 ± 0.02	–	–	S
63	J045538.99-662550.2	0.3	1.55 ± 0.10	-0.06 ± 0.08	0.91 ± 0.04	B, H, S
64	J045539.69-662959.5	0.5	7.50 ± 0.24	-0.28 ± 0.04	0.42 ± 0.04	B, S, H
65	J045540.12-662013.1	1.4	0.21 ± 0.05	1.00 ± 0.13	–	B, H
66	J045540.68-662613.3	0.5	0.12 ± 0.03	–	–	B, H, S
67	J045540.79-662820.1	0.6	0.05 ± 0.02	–	–	S
68	J045542.24-662610.2	0.4	0.18 ± 0.03	0.47 ± 0.19	–	B, H, S
69	J045542.82-663114.5	0.7	0.35 ± 0.05	-0.11 ± 0.18	0.70 ± 0.19	B, S, H
70	J045543.08-663303.6	1.3	0.29 ± 0.05	0.60 ± 0.16	–	B, H
71	J045544.02-662453.1	2.6	0.06 ± 0.02	–	–	S
72	J045549.27-662654.4	0.4	0.25 ± 0.05	–	–	B, H, S

Table 2—Continued

Source (1)	CXOU Name (2)	δ_x ($''$) (3)	CR (cts ks^{-1}) (4)	HR (5)	HR1 (6)	Flag (7)
73	J045549.98-663349.1	1.4	0.90 ± 0.09	-0.27 ± 0.13	0.59 ± 0.12	B, S, H
74	J045551.14-662050.7	1.2	0.20 ± 0.04	–	–	B, S, H
75	J045552.38-662850.9	0.5	0.16 ± 0.03	–	–	B, H, S
76	J045553.76-662831.5	0.3	0.69 ± 0.06	0.07 ± 0.11	0.96 ± 0.05	B, H, S
77	J045554.05-662459.2	1.0	0.05 ± 0.02	–	–	S
78	J045554.19-662818.9	0.3	0.68 ± 0.07	-0.30 ± 0.12	0.45 ± 0.12	B, S, H
79	J045554.52-662954.6	0.6	0.10 ± 0.03	–	–	S
80	J045554.56-661832.2	2.0	0.30 ± 0.06	–	–	B, S
81	J045554.75-662714.7	0.2	1.69 ± 0.10	-0.32 ± 0.07	0.59 ± 0.06	B, S, H
82	J045554.87-661701.0	2.4	1.69 ± 0.22	–	-0.07 ± 0.13	S, B
83	J045555.82-662709.8	2.3	0.04 ± 0.02	–	–	S
84	J045556.65-662223.0	0.6	1.22 ± 0.10	-0.05 ± 0.10	0.28 ± 0.11	B, S, H
85	J045556.89-663238.7	1.1	0.43 ± 0.07	0.12 ± 0.19	–	B, S, H
86	J045557.19-663130.5	0.8	0.57 ± 0.07	-0.28 ± 0.14	0.60 ± 0.14	B, S, H
87	J045558.10-661856.1	1.8	0.33 ± 0.07	–	–	S, B
88	J045601.44-662936.2	0.4	0.82 ± 0.07	-0.18 ± 0.11	0.44 ± 0.11	B, S, H
89	J045601.67-661901.8	1.9	0.28 ± 0.06	–	–	B, S
90	J045602.02-662616.3	1.3	0.07 ± 0.03	–	–	S
91	J045602.14-662643.8	0.7	0.06 ± 0.02	–	–	B
92	J045602.31-662403.2	0.6	0.05 ± 0.02	1.00 ± 0.04	–	H
93	J045602.53-662738.7	1.6	0.04 ± 0.02	–	–	S
94	J045604.12-662338.7	0.6	0.11 ± 0.03	–	–	B, S
95	J045604.18-662126.4	1.2	0.18 ± 0.05	–	–	S, B
96	J045604.40-662950.2	0.5	0.16 ± 0.03	–	0.89 ± 0.19	B, S
97	J045604.60-662358.0	0.7	0.10 ± 0.03	–	–	S, B
98	J045604.89-662638.7	1.3	0.06 ± 0.02	–	–	S
99	J045605.09-662807.5	0.4	0.19 ± 0.03	–	0.92 ± 0.13	B, S, H
100	J045605.21-662508.4	0.3	0.71 ± 0.06	0.16 ± 0.11	0.74 ± 0.11	B, H, S
101	J045606.08-661537.6	4.6	0.85 ± 0.32	–	–	S
102	J045606.31-662649.7	0.4	0.41 ± 0.05	0.15 ± 0.15	0.81 ± 0.14	B, H, S
103	J045607.45-663331.4	1.6	0.29 ± 0.06	–	–	B, S
104	J045608.01-662404.1	0.5	0.19 ± 0.04	–	–	B, S, H
105	J045608.50-662608.6	0.4	0.27 ± 0.04	0.61 ± 0.14	–	H, B, S
106	J045609.29-663455.5	2.2	0.19 ± 0.08	–	–	S
107	J045610.30-663046.6	0.9	0.18 ± 0.05	–	–	S, B
108	J045610.72-661938.7	2.0	0.16 ± 0.05	–	–	S

Table 2—Continued

Source (1)	CXOU Name (2)	δ_x ($''$) (3)	CR (cts ks^{-1}) (4)	HR (5)	HR1 (6)	Flag (7)
109	J045610.96-662359.5	0.7	0.12 ± 0.03	–	–	B, S
110	J045611.09-662824.6	0.6	0.04 ± 0.02	–	–	S
111	J045613.10-662123.9	1.2	0.21 ± 0.05	–	–	B, S
112	J045615.13-662410.9	0.5	0.32 ± 0.05	-0.11 ± 0.18	0.68 ± 0.17	B, S, H
113	J045617.78-662604.0	0.4	0.45 ± 0.05	-0.45 ± 0.14	0.61 ± 0.13	B, S, H
114	J045618.12-662721.0	0.5	0.22 ± 0.04	–	–	B, S, H
115	J045619.28-662702.3	0.7	0.09 ± 0.03	–	–	S
116	J045619.49-662631.0	0.4	1.56 ± 0.11	-0.10 ± 0.09	0.37 ± 0.09	B, S, H
117	J045620.14-662718.3	0.4	0.84 ± 0.07	0.17 ± 0.10	0.71 ± 0.11	B, H, S
118	J045620.37-663010.1	0.9	0.14 ± 0.04	–	–	B, S
119	J045621.49-662446.1	0.9	0.08 ± 0.03	–	–	S
120	J045622.48-662837.5	0.8	0.08 ± 0.03	–	–	B, H
121	J045622.87-663106.8	1.2	0.16 ± 0.04	–	–	S
122	J045623.18-662702.8	0.5	0.18 ± 0.04	0.62 ± 0.17	–	B, H
123	J045624.56-662206.7	0.9	3.78 ± 0.17	-0.32 ± 0.06	0.42 ± 0.05	B, S, H
124	J045625.33-663029.8	0.9	0.28 ± 0.05	–	-0.07 ± 0.20	S, B
125	J045626.22-662922.8	0.7	0.36 ± 0.06	-0.45 ± 0.19	0.39 ± 0.17	S, B
126	J045629.66-662138.5	1.5	0.18 ± 0.05	–	–	S
127	J045629.74-662702.7	0.6	1.41 ± 0.10	-0.21 ± 0.09	0.54 ± 0.09	B, S, H
128	J045629.82-662224.0	1.0	0.41 ± 0.06	–	0.40 ± 0.17	B, S
129	J045632.32-661905.4	2.1	0.53 ± 0.08	-0.04 ± 0.19	–	B, S, H
130	J045632.41-663012.9	1.0	0.34 ± 0.06	–	-0.07 ± 0.19	B, S
131	J045632.61-663506.2	2.8	0.46 ± 0.13	–	–	S, B
132	J045632.69-663100.5	1.2	0.26 ± 0.05	–	–	B, S
133	J045634.30-663035.3	1.1	0.43 ± 0.06	0.10 ± 0.15	0.88 ± 0.20	B, S, H
134	J045634.66-662827.2	0.8	0.27 ± 0.05	–	-0.04 ± 0.20	S, B
135	J045634.87-662623.1	0.7	0.54 ± 0.06	-0.15 ± 0.15	0.56 ± 0.14	B, S, H
136	J045636.28-663123.4	1.2	0.68 ± 0.08	-0.41 ± 0.15	0.43 ± 0.13	B, S, H
137	J045637.44-661829.9	2.3	1.26 ± 0.13	-0.19 ± 0.14	0.59 ± 0.13	B, S, H
138	J045639.99-663402.3	2.4	0.56 ± 0.11	–	–	B, S, H
139	J045640.74-662232.1	1.6	0.14 ± 0.04	1.00 ± 0.19	–	B, H
140	J045640.74-662655.7	0.8	0.73 ± 0.07	-0.07 ± 0.12	0.76 ± 0.12	B, S, H
141	J045642.55-662518.1	1.1	0.20 ± 0.05	–	-0.42 ± 0.19	S, B
142	J045643.20-662502.7	0.9	1.79 ± 0.13	-0.74 ± 0.09	-0.16 ± 0.07	B, S, H
143	J045643.77-662055.4	1.7	0.59 ± 0.08	-0.15 ± 0.18	0.53 ± 0.18	B, S, H
144	J045644.58-662921.1	1.4	0.16 ± 0.05	–	–	B

Table 2—Continued

Source (1)	CXOU Name (2)	δ_x ($''$) (3)	CR (cts ks^{-1}) (4)	HR (5)	HR1 (6)	Flag (7)
145	J045645.00-662858.9	1.4	0.15 ± 0.05	–	–	B
146	J045646.70-662446.6	1.1	0.37 ± 0.06	–	-0.03 ± 0.20	B, S
147	J045647.73-662752.5	1.1	0.44 ± 0.07	-0.48 ± 0.18	0.65 ± 0.17	B, S, H
148	J045648.22-662401.0	1.1	1.00 ± 0.08	0.15 ± 0.10	0.73 ± 0.11	B, H, S
149	J045649.22-663042.3	1.6	0.23 ± 0.05	–	–	B, S
150	J045651.35-661905.4	3.2	0.33 ± 0.11	–	–	S
151	J045655.52-663231.2	2.7	0.29 ± 0.09	–	–	B
152	J045658.75-662438.9	1.4	0.84 ± 0.09	-0.55 ± 0.19	-0.11 ± 0.11	B, S, H
153	J045659.64-662415.3	1.8	0.20 ± 0.05	–	–	B
154	J045700.03-662535.0	1.5	0.23 ± 0.05	–	–	B, H
155	J045700.05-662113.5	2.3	0.30 ± 0.07	–	–	B, H, S
156	J045700.53-662508.7	1.6	0.35 ± 0.07	–	–	B, S
157	J045700.94-662357.7	1.9	0.26 ± 0.06	–	–	S, B
158	J045702.07-662257.1	1.9	0.33 ± 0.06	0.42 ± 0.17	–	B, H
159	J045702.86-663042.3	1.9	0.45 ± 0.08	–	–	B, S
160	J045704.01-662131.9	2.1	0.95 ± 0.10	0.33 ± 0.10	–	B, H, S
161	J045705.85-661928.4	3.3	0.58 ± 0.14	–	–	B, H
162	J045706.90-662705.1	1.5	0.95 ± 0.10	-0.15 ± 0.12	0.65 ± 0.14	B, S, H
163	J045714.71-662226.7	2.3	1.07 ± 0.11	0.02 ± 0.13	0.83 ± 0.13	B, S, H
164	J045716.45-662322.6	2.5	0.34 ± 0.08	–	–	S, B
165	J045728.37-662232.0	3.9	0.52 ± 0.17	–	–	S

Note. — The energy bands were defined as follows: 0.3–0.7 (S1), 0.7–1.5 (S2), 1.5–3 (H1), and 3–7 keV (H2); S=S1+S2, H=H1+H2, and B=S+H. Column (1): Generic source number. (2): *Chandra* X-ray Observatory (unregistered) source name, following the *Chandra* naming convention and the IAU Recommendation for Nomenclature (e.g., http://cdsweb.u-strasbg.fr/iau-spec.html). (3): Position uncertainty (1σ) calculated from the maximum likelihood centroiding and an approximate off-axis angle (r) dependent systematic error $0\farcs2 + 1\farcs4 (r/8')^2$ (an approximation to Fig. 4 of Feigelson et al. (2002)), which are added in quadrature. (4): On-axis source broad-band count rate — the sum of the exposure-corrected count rates in the four bands. (5-6): The hardness ratios defined as HR = (H − S2)/(H + S2), and HR1 = (S2 − S1)/S, listed only for values with uncertainties less than 0.2. (7): The label "B", "S", or "H" mark the band in which a source is detected with the most accurate position that is adopted in Column (2).

Table 3. Properties of the OB stars detected in the X-ray domain

SRC	ELST	PGMW	Sp. Type	Bin.?	Count Rate (cts ks^{-1})	HR2	HR3	$N_{\rm H}$ (10^{22}cm^{-2})	log($L_{\rm BOL}$) ($L_\odot$)	$F_{\rm X}^{unabs}$ (10^{-15}erg cm^{-2}s^{-1})	log($L_{\rm X}/L_{\rm BOL}$)
48	004	–	OC9.7Ib	N	0.15 ± 0.04	–	–	0.48	5.80††	2.13±0.57	-6.58+-0.12
77	092	–	O7V	Y	0.05 ± 0.02	–	–	0.91	5.17	1.39±0.56	-6.13+-0.17
97	068	–	O7V	N	0.10 ± 0.03	–	–	0.10	5.06††	0.70±0.21	-6.32+-0.13
110	033	1005	B0IIIn	N	0.04 ± 0.02	–	–				
115	065	1027	O6.5V	N	0.09 ± 0.03	–	–	0.07	5.17††	0.59±0.20	-6.51+-0.15
126	051	–	O5Vn	N	0.18 ± 0.05	–	–	0.05	5.31††	1.13±0.31	-6.36+-0.12
134	†	†	WR+O		0.27 ± 0.05	-0.04 ± 0.20	–	0.00	6.29	2.04±0.38*	-7.09+-0.08
141	031	3061	ON2III	N	0.20 ± 0.05	-0.42 ± 0.19	–	0.65	5.84††	3.76±0.94	-6.37+-0.11
142	–	3070	O6V		1.79 ± 0.13	-0.16 ± 0.07	–	0.14	5.68	6.01±0.44*	-6.01+-0.03
146	–	3120	O5.5 V	C?	0.37 ± 0.06	-0.03 ± 0.20	–	0.50	5.88	2.97±0.48*	-6.51+-0.07
152	**	3204/9	O		0.84 ± 0.09	-0.11 ± 0.11	–	0.66	6.25	3.92±0.42*	-6.76+-0.05
157	050	3224	O4-5+O7	SB2	0.26 ± 0.06	-0.16 ± 0.22	–	0.91	5.66	7.22±1.67	-5.91+-0.10
163	120	–	B0.2Vn	Y	1.07 ± 0.11	0.83 ± 0.13	-0.04 ± 0.15				
164	028‡	3264	O6-8V	N	0.34 ± 0.08	–	–	0.89	5.65	3.11±0.73*	-6.26+-0.10
–	038	3100	O5III	N	0.07 ± 0.02	–	–	0.67	5.69††	1.36±0.39	-6.66+-0.12

Note. — Hardness ratios are here defined as HR3=(S4-S3)/(S3+S4) and HR4=(H4-H3)/(H4+H3) where S3, S4, H3 and H4 are the count rates in the 0.5–1, 1–2, 2–4, 4–8 keV bands, respectively (only quoted if their error are smaller than 1).

Exponents

∗ The flux was found from a spectral fit (see Table 4).

† This source corresponds to the HD32228 compound and comprises ELST25 [w21?,O8.5V], w30 [PGMW1210, O9Ib], w89 [PGMW1180, O8.5II(f)], w44 [PGMW1208, WC4], w62 [PGMW1198, O7.5III], w84 [PGMW1181, O9Vn], w50 [PGMW1212, O8V], w41 [PGMW1208, O9.5V], w51 [O9.5V], w68 [PGMW1198, O8.5V], w72 [PGMW1191, O9.5V] and w36 [O9V] - note that the w numbers are from Walborn et al. (1999). Of these, only w84 is a known SB2. The bolometric luminosity quoted in the tenth column is the sum of the individual luminosities, whereas the absorbing column (col 9) is the minimum one (see text).

∗∗ PGMW3204 corresponds to ELST48. The compound PGMW3204/9 is composed of ELST48 [O6.5V((f))], PGMW3209a [O3III(f*)], b [O9V], c [O7V], d [O9.5V], e [O9V] and f [O9.5V]. None of these objects is known as a binary. The bolometric luminosity quoted in the tenth column is the sum of the individual luminosities, whereas the absorbing column (col 9) is the average column of the PGMW3209 components.

‡ This star is the main object of N11A.

††The bolometric luminosity comes from the fits of Mokiem et al. (2007).

Table 4: Spectral properties of the brightest OB stars. Normalisation factors are defined as $(10^{-14}/4\pi D^2)\int n_e n_{\rm H} dV$ where D, n_e and $n_{\rm H}$ are, respectively, the distance to the source, the electron and proton density of the emitting plasma. The lower and upper limits of the 90% confidence interval are shown as indices and exponents, repectively, and fluxes are given in the 0.5–10 keV band.

SRC	$N_{\rm H}$ (10^{22}cm^{-2})	kT (keV)	norm (10^{-6}cm^{-5})	χ^2 (dof)	$F_{\rm X}$ (10^{-15}erg cm^{-2}s^{-1})	$F_{\rm X}^{unabs}$
134	$0._{0.}^{0.50}$	$1.30_{0.68}^{1.97}$	$2.37_{1.87}^{3.65}$	0.83 (6)	2.04	2.04
142	$0.89_{0.62}^{1.17}$	$0.57_{0.51}^{0.64}$	$19.7_{13.4}^{27.5}$	1.43 (19)	5.11	6.01
146	$0._{0.}^{0.16}$	$2.32_{1.63}^{3.78}$	$2.92_{2.32}^{3.53}$	1.57 (6)	2.97	2.97
152	$0.04_{0.}^{0.46}$	$1.34_{0.62}^{2.29}$	$4.76_{3.85}^{6.54}$	0.80 (10)	3.92	3.92
163	$1.43_{0.58}^{3.93}$	$70.3_{3.02}^{80.0}$	$10.4_{0.}^{13.6}$	0.75 (7)	14.0	
164	$0._{0.}^{2.23}$	$2.71_{0.44}^{80.0}$	$2.83_{0.}^{27.0}$	1.39 (2)	3.11	3.11

Table 5. Properties of the undetected O-type stars known in the field.

ELST	PGMW	Sp. type	Bin.?	$\log(L_{BOL}/L_\odot)$	$N_{\rm H}$ (10^{22} cm^{-2})	L_X^{unabs} (10^{32}erg s^{-1})	$\log(L_X/L_{BOL})$
007		O8 Ib (f)	N	5.72	0.58	<1.14	< -7.25
010	1310	O9.5 III + B1-2:	SB2	5.42	0.29	<0.78	< -7.11
011		OC9.5 II	SB1	5.49	0.43	<0.50	< -7.38
013	3223	O8 V	SB2	5.66	0.48	<1.74	< -7.00
018	3053	O6 II(f$^+$)	N	5.64	0.43	<1.15	< -7.16
019		O8-9 III-V((f))	SB2	5.40	0.24	<0.96	< -7.00
020		O5 I(n)fp	Y	5.50	0.14	<0.89	< -7.13
022		O6.5 II(f) var	N	5.45	0.29	<0.22	< -7.69
026		O2.5 III(f*)	N	5.92*	0.26	<1.74	< -7.26
029		OC9.7 Ib	N	5.21*	0.34	<0.30	< -7.32
032	3168	O7 II(f)	N	5.43*	0.38	<1.39	< -6.87
041		O6.5 Iaf	Y	5.17	0.19	<1.50	< -6.58
043	1519	O7 III + B0:	SB2	5.12	0.14	<0.92	< -6.74
045		O9-9.5 III	N	5.15*	0.26	<1.34	< -6.60
046		O9.5 V	Y	4.91	0.05	<1.75	< -6.25
049	1110	O7.5 V	SB1	5.04	0.07	<0.32	< -7.12
052		O9.5 V	SB2	4.95	0.19	<5.46	< -5.80
058		O5.5 V((f))	N	5.27*	0.12	<1.11	< -6.81
059	1125	O9 V	SB1	4.84	0.05	<0.41	< -6.81
060	3058	O3 V((f*))	N	5.57*	0.53	<1.42	< -7.00
061		O9 V	N	5.20*	0.50	<4.27	< -6.15
063		O9: Vn	SB2	4.88	0.22	<5.55	< -5.72
071		O8: V	SB2	4.84	0.19	<2.54	< -6.02
080	3173	O7: V + O9:	SB2	4.91	0.29	<0.90	< -6.54
087		O9.5 Vn	N	4.91*	0.38	<0.85	< -6.56
091		O9 V	Y	4.78	0.41	<2.50	< -5.97
108		O9.5 V	N	4.56	0.19	<1.42	< -5.99
122		O9.5 V	N	4.37	0.00	<0.36	< -6.40
123		O9.5 V	N	4.58*	0.02	<0.59	< -6.40
	1194	O9.5:IV		4.92	0.29	<0.58	< -6.74

Table 5—Continued

ELST	PGMW	Sp. type	Bin.?	$\log(L_{BOL}/L_{\odot})$	$N_{\rm H}$ (10^{22} cm^{-2})	L_X^{unabs} (10^{32}erg s^{-1})	$\log(L_X/L_{BOL})$
	1200	O6:V:p	C?	5.65	0.89	<2.13	< -6.90
	1239	O7-O8:V:		4.90	0.24	<0.81	< -6.57
	1288	O9 V		4.45	0.12	<0.60	< -6.25
	1292	O9:III:		4.67	0.77	<1.68	< -6.03
	1363	O8.5 Iaf		5.63	0.41	<1.34	< -7.09
	1365	O9 V		4.47	0.05	<0.58	< -6.29
	1377	O8:V		4.73	0.12	<0.70	< -6.47
	1388	O9.7 Iab		5.70	0.36	<1.38	< -7.14
	1396	O7 Vp		5.24	0.14	<0.81	< -6.92
	1431	O9 V		4.58	0.14	<0.71	< -6.31
	1481	O7 V((f))		5.22	0.17	<1.05	< -6.78
	1483	O6.5 III(f)		5.59	0.24	<1.18	< -7.10
	1486	O6.5 V		5.07	0.14	<0.86	< -6.72
	3016	O9.5:V		4.68	0.34	<0.91	< -6.30
	3045	O9.5 III		4.55	0.36	<0.87	< -6.19
	3073	O6.5 V		5.00	0.41	<1.62	< -6.37
	3089	O8 V		4.91	0.36	<0.98	< -6.50
	3102	O7 V		5.44	0.41	<1.58	< -6.83
	3103	O9.5:IV:		4.29	0.29	<1.00	< -5.87
	3115	O9 V		4.67	0.41	<1.70	< -6.02
	3123	O8.5 V		4.92	0.38	<1.18	< -6.43
	3126	O6.5 V		5.28	0.65	<1.66	< -6.64

*The bolometric luminosity comes from the fits of Mokiem et al. (2007).

Table 6. Spectral properties of the diffuse X-ray sources. Normalisation factors are defined as $(10^{-14}/4\pi D^2)\int n_e n_{\rm H} dV$ where D, n_e and $n_{\rm H}$ are, respectively, the distance to the source, the electron and proton density of the emitting plasma. The lower and upper limits of the 90% confidence interval are shown as indices and exponents, repectively, and fluxes are given in the 0.3–2 keV band.

Name	RA (hh:mm:ss)	DEC (°:′:″)	Semi-axes (″×″)	Pos. angle (°)	$N_{\rm H}$ (10^{22}cm^{-2})	kT (keV)	norm (10^{-5}cm^{-5})	χ^2 (dof)	$F_{\rm X}$ (10^{-14}	$F_{\rm X}^{unabs}$ erg cm^{-2}s^{-1})
north	04:55:53.2	−66:16:39.4	84.1×69.4	0	$0._{0.}^{0.001}$	$0.25_{0.18}^{0.34}$	$3.02_{1.66}^{7.38}$	1.00 (21)	2.16	2.16
middle	04:56:19.9	−66:21:46.2	233.2×138.7	0	$0.66_{0.53}^{0.76}$	$0.19_{0.18}^{0.21}$	$343.5_{187.9}^{535.0}$	1.60 (106)	16.1	194.8
middle-w	04:55:54.6	−66:22:21.8	106.6×66.1	58.9	$0.59_{0.39}^{0.76}$	$0.20_{0.18}^{0.24}$	$61.5_{26.2}^{159.}$	1.30 (81)	4.34	37.5
middle-se	04:56:45.7	−66:22:07.9	124.0×66.4	0	$0.46_{0.26}^{0.72}$	$0.24_{0.19}^{0.28}$	$32.5_{15.5}^{80.4}$	1.02 (84)	4.79	22.6
middle-ne	04:56:22.6	−66:20:32.4	63.7×63.7	0	$0.77_{0.36}^{1.04}$	$0.19_{0.15}^{0.29}$	$50.5_{7.58}^{169.}$	1.23 (66)	1.91	29.3
LH10†	04:56:44.8	−66:24:56.2	36.1×28.2	322.9	$0.32_{0.}^{0.97}$	$0.21_{0.19}^{0.40}$	$3.29_{1.10}^{53.7}$	1.36 (63)	0.97	2.84
						$2.77_{1.53}^{80.}$	$1.02_{0.57}^{1.35}$			
east of LH9	04:57:07.8	−66:26:52.2	53.1×73.8	323.7	$0.64_{0.49}^{0.90}$	$0.18_{0.15}^{0.25}$	$40.8_{8.20}^{153.}$	1.58 (77)	1.80	22.4
west of LH9	04:56:02.8	−66:30:28.9	118.1×67.9	0	$0.67_{0.54}^{0.79}$	$0.18_{0.16}^{0.19}$	$209._{91.7}^{471.}$	1.56 (105)	7.75	112.
LH9†	04:56:35.6	−66:28:34.8	178.8×106.2	21.3	$0._{0.}^{0.20}$	$0.23_{0.21}^{0.25}$	$24.3_{21.0}^{55.6}$	1.27 (117)	23.8	23.8
						$0.78_{0.72}^{0.88}$	$7.18_{5.21}^{8.36}$			
inside LH9**	04:56:56.3	−66:28:53.6	29.5×29.5	0	$0._{0.}^{2.25}$	$21.9_{2.62}^{80.}$	$0.48_{0.26}^{0.87}$	1.13 (55)	0.26	0.26
near HD32228**	04:56:34.7	−66:28:27.2	5.–15*		$1.36_{0.92}^{2.09}$	$0.71_{0.53}^{0.97}$	$1.23_{0.61}^{2.24}$	1.15 (67)	0.21	1.29

Note. — Exponents

$*$ Annulus of inner radius $5''$ and outer radius $15''$. The full spectrum of LH9 (see above) excludes a region of $15''$ around HD32228 and the spectrum of the X-ray point source associated with HD32228, extracted in the $5''$ region surrounding the star, was presented in Table 4. This annular region thus provides a study of the close neighbourhood of HD32228.

$\dagger$ Two-temperature plasmas were necessary to fit the spectra of these sources. The model thus has the form vphabs*(mekal+mekal)+wabs*mekal+wabs*pow, and the parameters of the second mekal are given in the second line.

$**$ The background for these regions were chosen as annuli surrounding the sources (see Fig. 9).